

# M4-SAR: A Multi-Resolution, Multi-Polarization, Multi-Scene, Multi-Source Dataset and Benchmark for optical-SAR Fusion Object Detection

Chao Wang<sup>ib</sup> *Student Member, IEEE*, Wei Lu<sup>ib</sup>, Xiang Li, Jian Yang, Lei Luo

**Abstract**—Single-source remote sensing object detection using optical or SAR images struggles in complex environments. Optical images offer rich textural details but are often affected by low-light, cloud-obscured, or low-resolution conditions, reducing the detection performance. SAR images are robust to weather, but suffer from speckle noise and limited semantic expressiveness. Optical and SAR images provide complementary advantages, and fusing them can significantly improve the detection accuracy. However, progress in this field is hindered by the lack of large-scale, standardized datasets. To address these challenges, we propose a new comprehensive dataset for optical-SAR fusion object detection, named Multi-resolution, Multi-polarization, Multi-scene, Multi-source SAR dataset (M4-SAR). It contains 112,174 precisely aligned image pairs and nearly one million labeled instances with arbitrary orientations, spanning six key categories. To enable standardized evaluation, we develop a unified benchmarking toolkit that integrates six state-of-the-art multi-source fusion methods. Additionally, we propose E2E-OSDet, a novel end-to-end multi-source fusion detection framework that mitigates cross-domain discrepancies and establishes a robust baseline for future studies. Extensive experiments on M4-SAR demonstrate that fusing optical and SAR data can improve mAP by 5.7% over single-source inputs, with particularly significant gains in complex environments. The dataset and code are publicly available at <https://github.com/wchao0601/M4-SAR>.

**Index Terms**—Remote sensing, benchmark, dataset, multi-source object detection, synthetic aperture radar.

## I. INTRODUCTION

WITH the rapid development of deep learning techniques, single-source detection (e.g., optical [1], [2] or synthetic aperture radar (SAR) [3]), and multi-source detection (optical-SAR [4], [5]) have garnered significant attention in the remote sensing field. These methods have demonstrated remarkable effectiveness in applications, including disaster monitoring and urban planning. As shown in Fig. 1 (c), optical images provide high-resolution visual cues with rich texture, color, and spectral information, facilitating fine-grained feature extraction and semantic interpretation under clear atmospheric

conditions. However, their detection performance degrades markedly under low-light, cloud-obscured, or low-resolution conditions (see Fig. 1 (a)). Despite these drawbacks, the intuitive appearance and broad availability of optical data have fueled significant advancements in optical image object detection [6]–[9]. In contrast, SAR sensors enable all-weather, all-day imaging, resilient to cloud cover and illumination changes. However, the inherent speckle noise and low contrast arising from microwave backscatter present significant obstacles to precise localization and classification. Moreover, constructing large-scale SAR datasets [10]–[12] is hindered by the high cost of data acquisition and the laborious fine-grained annotation. Although optical and SAR images exhibit strong complementarity in spatial resolution and environmental robustness, existing single-source [13]–[16] and multi-source approaches [17], [18] face challenges in addressing cross-domain distribution shifts and suffer from the absence of a standardized evaluation benchmark. To enable robust detection in complex scenarios, there is an urgent need for a large-scale, precisely aligned optical-SAR fusion detection dataset and a standardized benchmarking toolkit.

Currently, a major bottleneck in optical-SAR fusion object detection lies in the lack of large-scale, high-quality, and standardized datasets. As shown in Table I, most existing SAR datasets are limited to single-source data, suffering from limited scale, narrow category coverage, or inconsistent annotations. For example, HRSID [19], SADD [20], SSDD [21], SIVED [22], and ShipDataset [23] exhibit notable limitations in terms of category diversity and dataset scale. In recent years, the emergence of larger-scale datasets such as SARDet-100K [10], FAIR-CSAR [12], and RSAR [11] has partially addressed these limitations. However, these datasets are often synthesized by standardization of data from multiple sources, potentially introducing bias during data preprocessing and compromising the fairness of model evaluation. Moreover, constructing paired optical-SAR datasets is prohibitively expensive: acquiring SAR data is already costly, and the acquisition of spatio-temporally aligned optical images is even more difficult, further limiting the construction of multi-source datasets.

Although OGSOD-1.0 [24] and OGSOD-2.0 [25] represent pioneering efforts in optical-SAR multi-source data, they are primarily designed for cross-modal knowledge distillation. Moreover, their test sets consist solely of SAR images, which limits their applicability for end-to-end multi-source fusion object detection. To address this issue, we constructed the novel optical-SAR fusion object detection dataset (M4-SAR)

This work was supported in part by the National Natural Science Foundation of China (No. 62276135, and 62361166670). (Corresponding author: Lei Luo)

Chao Wang, Yanguang Sun, Jian Yang and Lei Luo are with the PCA Laboratory, Key Laboratory of Intelligent Perception and Systems for High-Dimensional Information of Ministry of Education, School of Computer Science and Engineering, Nanjing University of Science and Technology, Nanjing 210094, China (Email: wchao0601@163.com, csjyang@njust.edu.cn, luoleipitt@gmail.com).

Wei Lu is with the MOE Key Lab of ICSP, Anhui University, Hefei, China (Email: luwei\_ahu@qq.com).

Xiang Li is with the College of Computer Science, Nankai University, Tianjin, China (Email: xiang.li.implus@nankai.edu.cn).

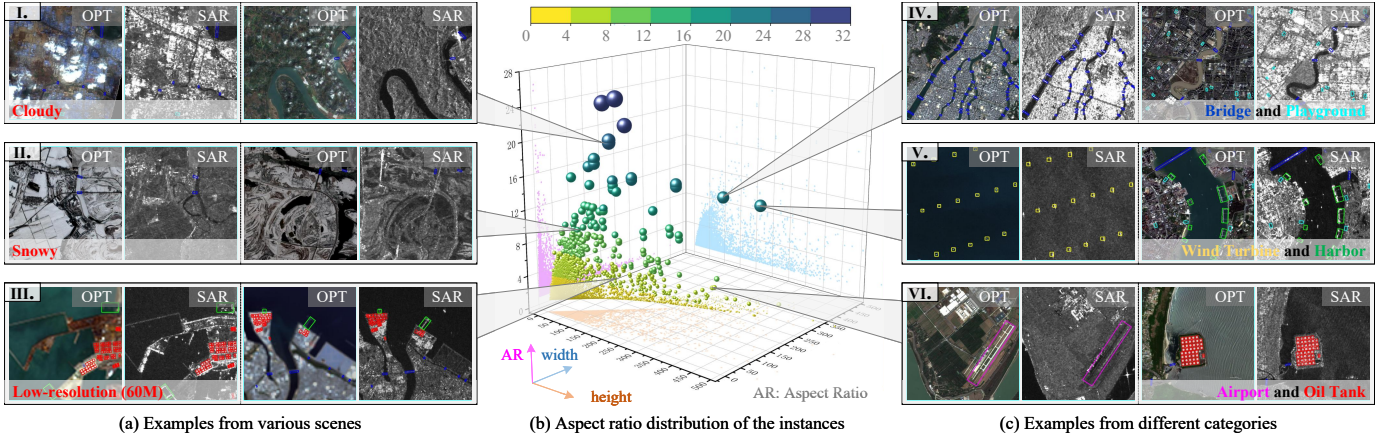


Fig. 1. Examples of scenes and six key target categories in the proposed M4-SAR dataset, accompanied by instance size and aspect ratio distributions.

covering multi-resolution, multi-polarization, multi-scene, and multi-source using publicly available optical and SAR data provided by Sentinel-1 [26], and Sentinel-2 [27] satellites. To overcome SAR annotation challenges, we propose a semi-supervised optical-assisted labeling strategy that utilizes optical images’ semantic richness to substantially improve annotation quality. As illustrated in Fig. 1 and Table I, M4-SAR includes six key target categories with 112,174 image pairs and 981,862 instances. M4-SAR surpasses existing datasets in instance volume and alignment precision, establishing a robust benchmark for multi-source fusion in complex scenarios.

Another important challenge is the lack of publicly available algorithms tailored for optical-SAR fusion object detection. Most existing studies are based on single-source datasets or evaluated on limited scenarios, making it difficult to conduct fair performance comparisons. To bridge this gap, we introduce Multi-Source Rotated Object Detector (MSRODet), an open-source toolkit that integrates state-of-the-art fusion detectors (e.g., CFT [28], CLANet [17], CSSA [18], CMADet [29], ICAFusion [30], and MMIDet [31]), providing a standardized evaluation framework for researchers utilizing the M4-SAR dataset. MSRODet not only enables fair and reproducible benchmarking across different fusion methods but also lays a solid foundation for the development of future multi-source fusion object detection algorithms.

Moreover, extensive experiments demonstrate that the intrinsic differences in the imaging mechanisms of optical and SAR sensors lead to significant domain gaps (Fig. 4 (a)), thereby constraining the performance of optical-SAR fusion object detection. To address this issue, we propose the first end-to-end framework for optical-SAR fusion object detection, termed E2E-OSDet. This framework effectively fuses features from both modalities, alleviates cross-modal domain gaps, and results in significant improvements in both inference speed and detection performance.

This work offers substantial contributions in terms of dataset construction, toolkit development, and algorithm design. The main contributions of this work are summarized as follows:

- **M4-SAR Dataset:** M4-SAR is a novel optical-SAR fusion object detection dataset with multi-resolution, multi-polarization, and multi-scene characteristics, containing

112,174 image pairs and 981,862 instances. This dataset comprehensively covers complex scenes and diverse target categories frequently encountered in multi-source fusion detection tasks, thereby providing a robust foundation for advancing research in this field.

- **Multi-source Evaluation Toolkit (MSRODet) and E2E-OSDet:** We introduce MSRODet, a comprehensive benchmarking toolkit incorporating state-of-the-art fusion methods tailored for optical-SAR object detection, which provides a standardized and reproducible evaluation platform based on the M4-SAR dataset. In addition, we propose E2E-OSDet, a novel end-to-end optical-SAR fusion object detection framework, which effectively mitigates significant cross-domain discrepancies between optical and SAR modalities at the feature level.

## II. RELATED WORK

### A. Related Datasets

Progress in SAR object detection is impeded by the high costs of data acquisition and the intricacy of fine-grained annotation. Consequently, existing datasets, including HRSID [19], SADD [20], SSDD [21], and SIVED [22], are frequently restricted to a limited number of common categories (e.g., ships), generally comprising fewer than 10,000 images with constrained class diversity (Table I). These constraints impede the development of robust and generalizable models for remote sensing applications. Recent efforts have sought to tackle these challenges. Wang et al. [23] introduced the Ship-Dataset, which comprises 39,729 ship patches extracted from Gaofen-3 and Sentinel-1 imagery, extensive in scale but constrained in semantic diversity. Xia et al. [32] introduced MSAR, broadening the categories to include airplanes, tanks, bridges, and ships. To address data scarcity, Li et al. [10] released SARDet-100K, comprising 116,598 images and 245,653 instances across six categories. Wu et al. [12] contributed FAIR-CSAR, providing fine-grained multi-domain annotations, while Zhang et al. [11] enhanced annotation efficiency in RSAR through weakly supervised learning and rotated bounding boxes.

Despite these advancements, which signify a shift from small-scale, single-category collections to large-scale, multi-class benchmarks, most existing datasets remain restricted to

TABLE I  
COMPARISON BETWEEN EXISTING OPTICAL AND SAR OBJECT DETECTION DATASETS AND THE PROPOSED M4-SAR DATASET.

Dataset	OPT	SAR	Spatial Resolution	Polarization	Image Size	Category	Instances	Images	Ins/Img
HRSC2016 [6]	✓	✗	0.4M ~ 2M	-	300 ~ 1,500	1	2,976	1,061	2.80
LEVIR [7]	✓	✗	0.2M ~ 1M	-	600 × 800	3	11,028	21,952	0.50
DIOR-R [8]	✓	✗	0.5M ~ 30M	-	800 × 800	20	190,288	23,463	8.11
DOTA-v1.0 [9]	✓	✗	-	-	800 ~ 4,000	15	188,282	2,806	67.10
HRSID [19]	✗	✓	-	HH, HV, VH, VV	800 × 800	1	16,969	5,604	3.03
SADD [20]	✗	✓	-	HH	224 × 224	1	7,835	883	8.87
SSDD [21]	✗	✓	-	HH, HV, VH, VV	512 × 512	1	2,587	1,160	2.23
SIVED [22]	✗	✓	-	VV, VH	512 × 512	1	12,013	1,044	11.51
ShipDataset [23]	✗	✓	-	HH, HV, VH, VV	256 × 256	1	50,885	39,729	1.28
MSAR [32]	✗	✓	-	HH, HV, VH, VV	256 × 256	4	65,202	30,158	2.16
SARDet-100K [10]	✗	✓	-	HH, HV, VH, VV	512 × 512	6	245,653	116,598	2.11
FAIR-CSAR [12]	✗	✓	-	HH, HV, VH, VV	1,024 × 1,024	5	349,002	106,672	2.11
RSAR [11]	✗	✓	-	HH, HV, VH, VV	512 × 512	6	183,534	95,842	1.91
OGSOD-1.0 [24]	✓	✓	20M	VV, VH	256 × 256	3	48,589	18,331	2.65
OGSOD-2.0 [25]	✓	✓	20M	VV, VH	256 × 256	3	54,000	20,359	2.65
<b>M4-SAR (Ours)</b>	✓	✓	<b>10M, 60M</b>	<b>VV, VH</b>	<b>512 × 512</b>	<b>6</b>	<b>981,862</b>	<b>112,174</b>	<b>8.75</b>

single-source data. Consequently, they cannot exploit complementary multimodal information critical for robust object detection in real-world remote sensing scenarios. Although OGSOD-1.0 [24] and OGSOD-2.0 [25] offer aligned optical-SAR image pairs, their evaluation protocol depends solely on SAR data, limiting their applicability for end-to-end fusion-based detection. Thus, there is an urgent need for a high-quality multi-source dataset that enables comprehensive optical-SAR fusion object detection.

### B. Remote Sensing Object Detection

Remote sensing images, encompassing both optical and synthetic aperture radar (SAR) modalities, pose distinct challenges for object detection. SAR imagery is particularly susceptible to multiplicative speckle noise and structural distortions, which hinder reliable feature extraction. Early approaches sought to address these challenges using handcrafted descriptors, including the Canny edge detector [33], Wavelet Scattering Transform (WST) [34], Haar-like features [35], Histogram of Oriented Gradients (HOG) [36], and Gradient-by-Ratio edge detection (Grad) [37]. These methods capture structural information through edge detection, frequency decomposition, or gradient statistics, and have been effectively adapted for both optical and SAR targets. However, their constrained representation capacity and susceptibility to imaging conditions limit their performance in complex remote sensing environments.

With the advent of deep learning, object detection has attained remarkable advancements. Architectures such as R-CNN [38], [39], YOLO [40]–[43], and DETR have exhibited robust generalization across natural images, with numerous variants adapted for remote sensing data. Nevertheless, SAR object detection remains formidable due to speckle noise and the absence of rich semantic cues. To tackle these challenges, recent studies have developed SAR-specific designs. For instance, the SFS-Conv [44] employs fractional Gabor transforms to enhance frequency-domain representations, while SAR-JEPA [37] introduces a joint embedding framework that predicts multi-scale gradient features through masked local reconstruction. The large-margin anomaly detection model [45] facilitates cross-modal generalization between optical and SAR data by learning a deviation metric independent of the

background distribution. Wang et al. developed a lightweight SAR ship detection network through evolutionary strategies [46], demonstrating the potential of resource-efficient architectures. Beyond these task-specific advancements, foundational SAR understanding models such as SARATR-X [47] reveal that self-supervised pretraining on large-scale SAR datasets produces highly transferable feature representations.

Despite these advancements, most existing methods are tailored for single-source SAR data and fail to leverage the complementary strengths of auxiliary modalities, such as optical images. This constraint underscores the need for multi-source fusion methods capable of exploiting optical-SAR synergy to reduce noise, enhance semantic context, and improve detection robustness in complex remote sensing scenarios.

### C. Multi-source Fusion Object Detection

Deep neural networks, due to their strong nonlinear modeling capacity, have significantly advanced multi-source fusion object detection [18], [29], [30]. Recent studies have tackled key challenges in cross-modal integration. For example, Yuan et al. [48] and Fang et al. [28] proposed alignment strategies to mitigate spatial misalignments between heterogeneous modalities. He et al. [17] investigated semantic conflicts and complementarity across sources to enhance fusion effectiveness. Zeng et al. [31] introduced a contour enhancement module to extract modality-specific spectral features from visible and infrared images, emphasizing spatial diversity and fine-grained structures. Despite these advances, many existing frameworks suffer from complex training procedures, limiting scalability and real-world deployment. To address this, Zhang et al. [49] proposed E2E-MFD, an end-to-end architecture that streamlines the fusion pipeline through a single-stage training process while achieving strong performance.

However, the majority of prior research has focused on visible–infrared or multispectral–RGB fusion, while optical–SAR fusion remains relatively underexplored. This setting poses unique challenges due to significant disparities in feature distributions and sensing mechanisms. Optical images offer rich color and texture cues but are sensitive to lighting and weather, whereas SAR data provides geometric and structural information resilient to environmental changes. Effectively

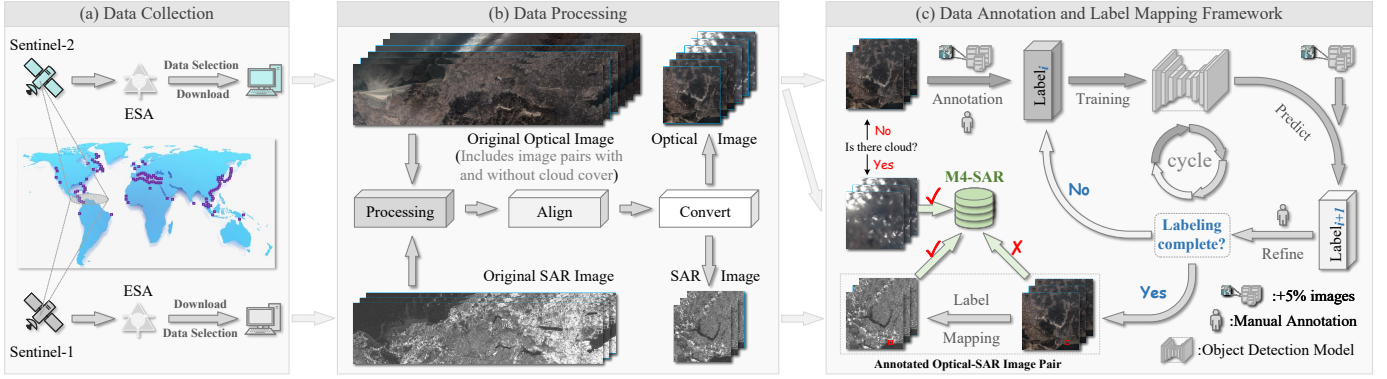


Fig. 2. Pipeline for M4-SAR dataset construction.

integrating these complementary properties is essential for robust object detection in complex remote sensing scenarios. The lack of large-scale, high-quality optical-SAR datasets and specialized fusion algorithms highlights an urgent need for new methods tailored to this modality pair.

### III. M4-SAR DATASET

#### A. Overview of the Proposed Dataset Construction Pipeline

Fig. 2 illustrates the overall pipeline of the proposed dataset construction process. In the first stage, we acquire optical and SAR images from Sentinel-1 and Sentinel-2 satellites provided by the European Space Agency (ESA). In the second stage, the acquired images are pre-processed and aligned. After completing the alignment, we crop aligned image pairs into fixed-size patches to generate initial unlabeled samples. In the third stage, we introduce a semi-supervised annotation strategy guided by optical images to ensure high-quality labeling of the image pairs.

#### B. Data Collection Procedure

First, we collected the required data via the open-access platform provided by the ESA. A map-based selection tool was used to specify areas of interest, covering representative coastal cities, including Tianjin, Los Angeles, Hong Kong, and London. We then retrieved SAR images along with their corresponding digital elevation model (DEM) data according to specific criteria. For optical imagery, Sentinel-2 images covering the same regions as the Sentinel-1 data were acquired, specifically including the red (R), green (G), and blue (B) spectral bands. To minimize variations caused by temporal discrepancies between the two modalities, we selected image pairs with a time interval of less than 10 days. This setting ensures that targets of interest (e.g., bridges, oil tanks) maintain structural consistency within the short interval, thereby enhancing the accuracy of subsequent instance-level alignment. The product type for optical images is L2A, with cloud coverage limited to 0–10% (the corresponding cloud-free (0%) images are used for high-quality annotation) to guarantee high visual fidelity. The SAR images are provided in the Single Look Complex (SLC) format to preserve full coherence information. The collected data span the period from 2020 to 2022 and encompass multiple spatial resolutions

and polarization modes. The optical images have 10m, 20m, and 60m resolutions, and the SAR data cover both vertical-horizontal (VH) and vertical-vertical (VV) polarizations.

#### C. Data Processing

We combined the red, green, and blue channels to generate standard optical images using data processing software. The optical images were provided in three spatial resolutions: 10m, 20m, and 60m. To highlight the complementary characteristics of optical and SAR images, we retained only the high-resolution (10m) and low-resolution (60m) variants. For the SAR data, we first applied multi-look averaging to the SLC images in both the azimuth and range directions to reduce speckle effects and improve radiometric resolution. Subsequently, filtering techniques were employed to suppress speckle noise. Using the corresponding DEM data, we geocoded and radiometrically calibrated the SAR images and conducted geometric alignment and correction to improve spatial localization precision. After preprocessing, the optical and SAR images were aligned based on their geographic coordinates. As the overlap between the two modalities was partial, the aligned image pairs were cropped into  $1,024 \times 1,024$  patches, and only those with valid overlapping regions were retained for subsequent annotation. Notably, this initial cropping was intended to facilitate efficient manual annotation. After annotation was completed, we further partitioned the annotated images into non-overlapping  $512 \times 512$  tiles to meet the demands of different downstream applications.

#### D. Data Annotation and Label Mapping

As the acquisition times of Sentinel-1 [26] and Sentinel-2 [27] are not perfectly synchronized, instance-level alignment of dynamic targets (e.g., ships) becomes difficult, which compromises the accuracy of label transfer. To address this issue, we focus on static and semantically meaningful targets, such as bridges, harbors, oil tanks, playgrounds, airports, and wind turbines, and annotate them using oriented bounding boxes. SAR's unique imaging characteristics cause ambiguous target boundaries, challenging accurate annotation by non-experts. In contrast, optical images (cloudless) provide clearer visual cues that facilitate both target identification and annotation transfer. With precise alignment, annotations derived from



Fig. 3. Statistical visualization of category attributes in the proposed M4-SAR dataset. (a) Angle distribution of instances in each category. (b) Percentage of instances per category. (c) Average pixel area of instances per category.

optical images can be reliably transferred to SAR images, thereby significantly reducing manual annotation costs.

Given the scale of the dataset, fully manual labeling is both time-consuming and labor-intensive. To address this challenge, we propose a semi-supervised annotation strategy, as illustrated in Fig. 2 (c). The procedure involves the following steps: First, 5% of the entire cloudless optical images are manually annotated, ensuring that each selected image contains all six target categories: bridges, harbors, oil tanks, playgrounds, airports, and wind turbines. This subset establishes a high-quality foundation for subsequent annotation. Once manually labeled, a detector [40] is trained using this subset (with the same data used for both training and evaluation during the initial phase). The trained model is then employed to generate pseudo-labels for an additional 5% of the data, which are subsequently refined through manual correction and added to the labeled set. This updated set is used to retrain the detector in the next iteration. The annotation process is repeated iteratively until the full dataset is labeled. During this procedure, images without valid target instances are excluded to enhance annotation efficiency of the dataset.

During the annotation process, we use cloud-free images to ensure annotation accuracy. After annotation is complete, the cloud-free images are replaced with the corresponding cloud-containing images. Based on instance-level alignment, we achieve high-quality label transfer, enabling accurate projection of annotation information from optical images to their corresponding SAR counterparts. As a result, we construct M4-SAR, the large-scale dataset for optical-SAR fusion object detection, which offers a solid foundation for subsequent method evaluation and algorithm development.

### E. Statistical Analysis of Different Modalities

As shown in Table I, our proposed M4-SAR dataset comprises 112,174 image pairs, 981,862 instances, and six representative target categories: bridges, harbors, oil tanks, playgrounds, airports, and wind turbines. Each image has a resolution of  $512 \times 512$  pixels and contains an average of 8.75 instances, highlighting the dense object distribution typical in remote sensing scenes. As illustrated in Fig. 1 (c), rotated

bounding boxes offer significantly higher localization accuracy compared to horizontal bounding boxes.

Statistical analysis of category-specific attributes in the M4-SAR dataset is presented as follows:

- **Aspect Ratio:** The aspect ratio of an object plays a critical role in detection accuracy. Fig. 1 (b) illustrates the distribution of aspect ratios across categories. When the aspect ratio approaches 1, targets tend to appear square, potentially leading to recognition ambiguities. Conversely, extremely large aspect ratios increase the model’s sensitivity to object shapes, thus posing additional challenges to accurate detection.
- **Angle:** All target orientation angles are normalized to  $\theta$  ( $\theta \in [0, \pi/2)$ ), and their distributions are visualized in Fig. 3 (a). Notably, offshore wind turbines tend to exhibit square-like appearances, with orientation angles predominantly distributed around  $0^\circ$  and  $90^\circ$  due to the absence of surrounding reference structures and the top-down perspective of satellite imagery. Although oil tanks are circular, their labeled angles are contextually defined based on surrounding spatial features. This highlights the importance of contextual cues in remote sensing images and reflects the task’s sensitivity and complexity.
- **Number of Instances:** Fig. 3 (b) displays the distribution of instances by category, revealing that bridges and oil tanks constitute the largest proportions in the dataset. This imbalance reflects the actual occurrence frequency of typical targets in coastal regions: in such areas, static infrastructure such as bridges and oil tanks dominates satellite imagery. The relatively low number of port instances is primarily due to their extensive spatial coverage, with a single port typically corresponding to a single annotated instance.
- **Average Area of Objects:** Fig. 3 (c) shows the average pixel area per category, revealing the scale variability among different object categories in the dataset.

## IV. METHOD

### A. optical-SAR Fusion Detection Tools

Due to the lack of publicly available methods specifically designed for optical-SAR fusion object detection, conduct-

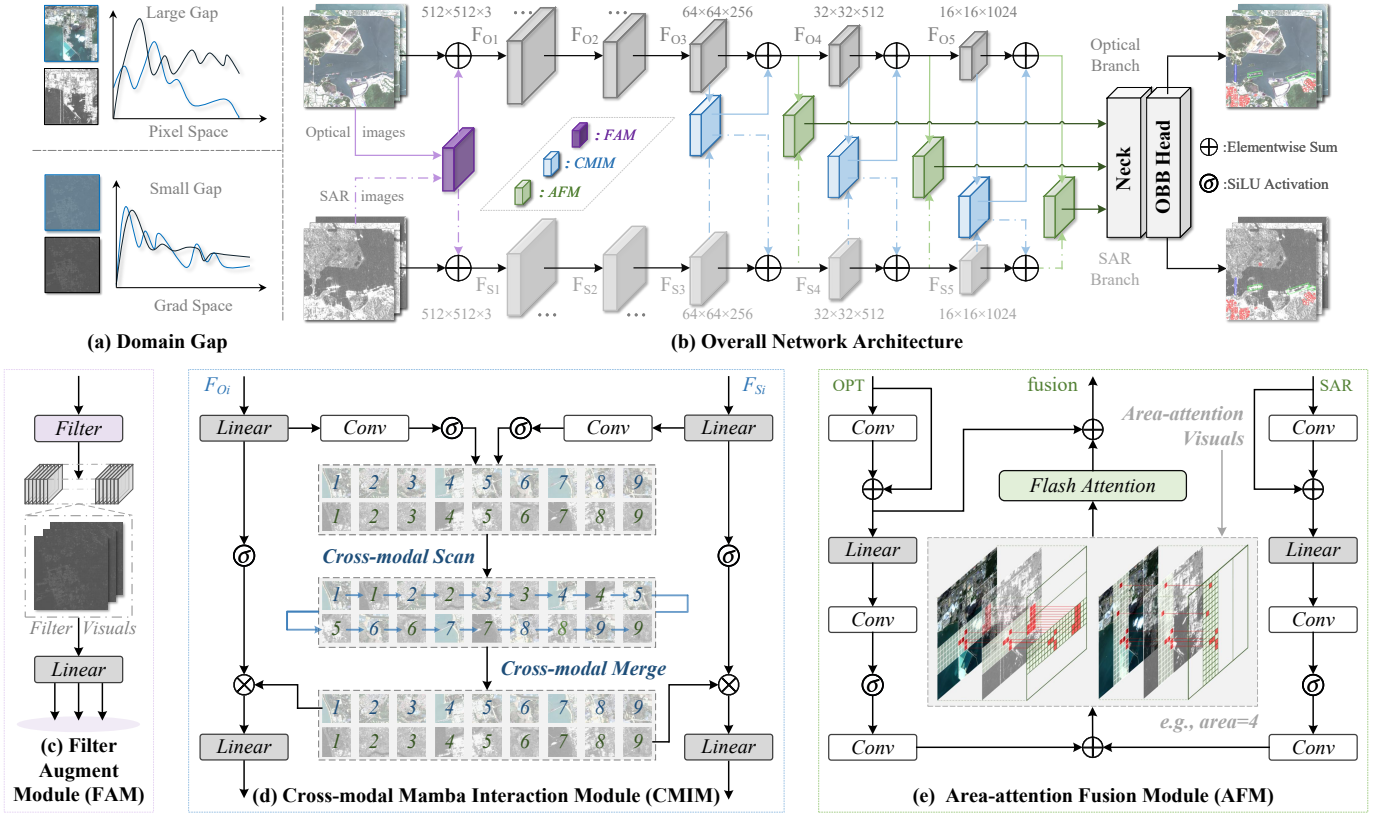


Fig. 4. (a) optical-SAR domain gap. (b) Overall framework of the proposed end-to-end optical-SAR fusion object detection (E2E-OSDet). Architectural details of the proposed filter augment module (c), cross-modal Mamba interaction module (d), and area-attention fusion module (e).

ing a fair performance comparison remains challenging. To address this limitation, we propose a Multi-Source Rotated Detector (MSRODet) built upon existing multi-source detection frameworks (e.g., RGB-infrared, RGB-depth). MSRODet integrates several representative methods, including CFT [28], CLANet [17], CSSA [18], CMADet [29], ICAFusion [30], and MMIDet [31], thereby providing a standardized and accessible benchmark for evaluating optical-SAR fusion object detection approaches. As shown in Fig. 4 (a), empirical analysis reveals that significant domain gaps remain a primary obstacle to effective optical-SAR fusion. These discrepancies primarily arise from fundamental differences in visual characteristics and imaging mechanisms between optical and SAR modalities. Consequently, designing detection frameworks specifically tailored to optical-SAR fusion is essential for enhancing overall detection performance.

### B. End-to-End optical-SAR Fusion Object Detection

1) *Overall Framework*: Multi-source fusion for object detection remains relatively underexplored in the context of optical-SAR integration, and notable challenges persist due to the significant domain discrepancies between the two modalities. As illustrated in Fig. 4 (b), we propose an end-to-end optical-SAR fusion framework, E2E-OSDet, which explicitly tackles these cross-modal challenges at three complementary levels: data input, domain alignment, and feature fusion.

2) *Filter Augment Module*: To address the inherent domain disparities between optical and SAR images, caused by

differences in imaging mechanisms and feature distributions, we propose the Filter Augment Module (FAM), a novel preprocessing framework designed to harmonize multi-source inputs for robust object detection. FAM incorporates a suite of classical image filtering operators, including HOG [36], Canny [33], Haar [35], Grad [37], and WST [34]. These filters extract complementary low-level cues, such as edges, gradients, and textures, under diverse imaging conditions. By projecting the sparse, low-dimensional features of both optical and SAR images into a high-dimensional, discriminative feature space, FAM reduces cross-modal domain gaps and enhances the alignment of modality-specific characteristics. Specifically, given an optical image  $I_O \in \mathbb{R}^{H \times W \times 3}$  and a SAR image  $I_S \in \mathbb{R}^{H \times W \times 1}$ , FAM generates a set of enhanced representations  $F_O \in \mathbb{R}^{H \times W \times 3}$  and  $F_S \in \mathbb{R}^{H \times W \times 1}$  for each filter  $t \in \{\text{WST, Canny, Haar, HOG, Grad}\}$ , defined as:

$$F_O = I_O + \alpha * \text{FAM}^t(I_O), \quad (1)$$

$$F_S = I_S + \alpha * \text{FAM}^t(I_S), \quad (2)$$

$$t \in \{\text{WST, Canny, Haar, HOG, Grad}\}, \quad (3)$$

where  $\text{FAM}^t(\cdot)$  denotes the  $t$ -th filter-specific augmentation function, and  $\alpha$  represents a set of learnable scalars that balance the contributions of the original and filtered features for the optical and SAR modalities, respectively. This dual-branch enhancement scheme preserves the structural and textural integrity of each modality while injecting noise-robust, multi-scale edge and shape cues derived from classical filters.

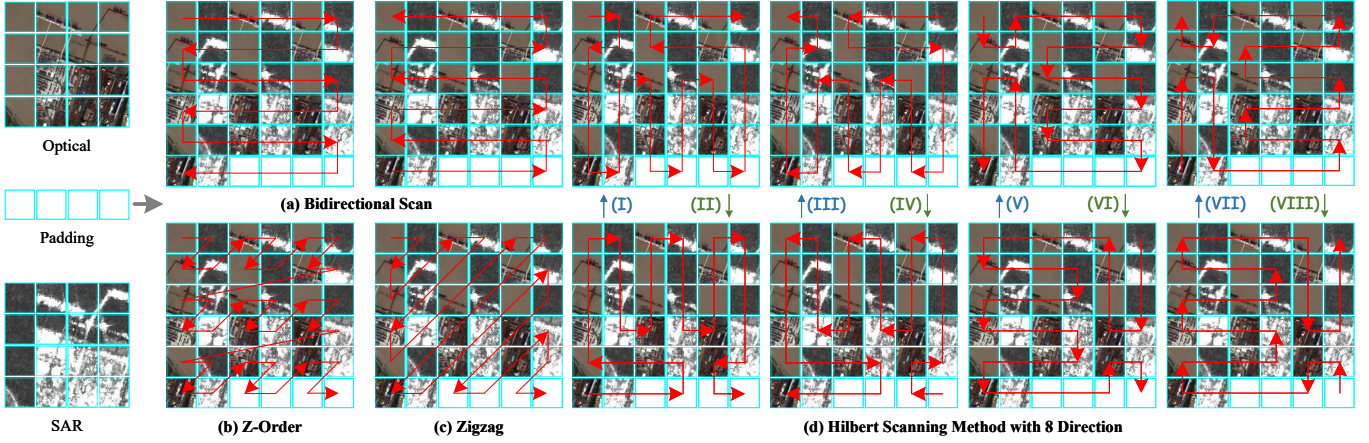


Fig. 5. The scanning mechanisms explored in this work include the Bidirectional Scan, Z-Order, Zigzag, and the 8-direction Hilbert Scanning Method.

By aligning feature representations across modalities at the preprocessing stage, FAM facilitates more effective optical-SAR fusion. It addresses the limitations of conventional preprocessing pipelines and significantly enhances the generalization capability of multi-source object detection models under diverse and challenging remote sensing conditions.

3) *Cross-modal Mamba Interaction Module*: Existing multi-source fusion methods primarily emphasize spatial-level feature integration, often neglecting the substantial domain discrepancies between heterogeneous modalities such as optical and SAR images. These domain shifts pose a significant challenge to effective cross-modal fusion. The Mamba framework [50], with its state-space modeling and efficient sequence processing capabilities, has demonstrated strong potential for capturing long-range dependencies. This makes it well-suited for mitigating inter-modal inconsistencies. However, existing Mamba-based fusion methods [51], [52] typically involve intricate architectures and computationally intensive interaction designs, which limit their scalability and practical deployment. To overcome these limitations, we propose the Cross-modal Mamba Interaction Module (CMIM), a lightweight yet powerful module tailored to align optical and SAR features by leveraging Mamba’s long-sequence modeling strength. Given paired image features ( $F_{Oj}, F_{Sj} \in \mathbb{R}^{\frac{H}{2^j} \times \frac{W}{2^j} \times C_j}, j \in \{3, 4, 5\}$ ), we first flatten them into one-dimensional sequences ( $X_j \in \mathbb{R}^{1 \times n}, Y_j \in \mathbb{R}^{1 \times n}$ ) in row-major order:

$$X_j = [p_1^o, p_2^o, \dots, p_{n-1}^o, p_n^o], Y_j = [p_1^s, p_2^s, \dots, p_{n-1}^s, p_n^s], \quad (4)$$

where  $p_i^o$  and  $p_i^s$  represent patches in optical and SAR imagery, respectively. Traditional methods concatenate these sequences to obtain  $Z_j^{tra} \in \mathbb{R}^{1 \times 2n}, j \in \{3, 4, 5\}$ :

$$Z_j^{tra} = [p_1^o, p_2^o, \dots, p_{n-1}^o, p_n^o, p_1^s, p_2^s, \dots, p_{n-1}^s, p_n^s]. \quad (5)$$

However, these sequence modeling methods often fail to establish explicit local correspondences between modalities, leading to suboptimal cross-modal alignment and feature fusion.

To address this issue, we introduce an **Interleaved Input Rearrangement (IIR)** mechanism that enforces fine-grained spatial correspondence by interleaving paired features in a one-to-one fashion. Specifically, given vectorized feature sequences

$X_j$  and  $Y_j$  from the optical and SAR modalities, respectively, IIR constructs a unified sequence  $Z_j^{IIR} \in \mathbb{R}^{1 \times 2n}$  by interleaving the features as:

$$Z_j^{IIR} = [p_1^o, p_1^s, p_2^o, p_2^s, p_3^o, p_3^s, \dots, p_{n-1}^o, p_{n-1}^s, p_n^o, p_n^s]. \quad (6)$$

This interleaving ensures that corresponding positional features from both modalities are adjacent, enabling Mamba’s state-space modeling to directly capture semantic and structural alignments, thus enhancing domain coherence. The resulting interleaved sequence is subsequently fed into a directional scanning mechanism (see Fig. 5 [53]), which applies Mamba blocks along both horizontal and vertical directions. This bi-directional sequence modeling allows CMIM to capture long-range dependencies while preserving fine-grained local correspondence, facilitating deeper cross-modal interaction. Finally, the output sequence is reshaped back into the 2D spatial domain and fused with residual skip connections to retain original modality-specific information. Through this design, CMIM effectively bridges modality gaps and enhances the robustness of multi-source object detection under challenging remote sensing conditions.

$$Z_j^{scan} = \text{SCAN}^m(Z_j^{IIR}), \quad (7)$$

$$m \in \{\text{Bid, Z-Order, Zigzag, Hilbert}\}. \quad (8)$$

The CMIM then transforms the scanned sequence into enhanced feature representations:

$$\{F'_{Oj}, F'_{Sj}\} = \text{CMIM}(Z_j^{scan}), \quad j \in \{3, 4, 5\}. \quad (9)$$

By positioning optical and SAR features adjacent along the temporal axis, the Interleaved Input Rearrangement (IIR) mechanism enables synchronous semantic enhancement within short time steps, effectively mitigating the risk of feature divergence during training. This temporal alignment facilitates efficient parameter sharing across modalities, stabilizes the training process, and promotes consistent gradient flow. As a result, IIR significantly enhances cross-modal feature alignment and consistently outperforms conventional fusion strategies in complex remote sensing scenarios.

TABLE II

QUANTITATIVE RESULTS ON THE M4-SAR. O AND S DENOTE OPTICAL AND SAR DATA, RESPECTIVELY. PARAM. DENOTES THE PARAMETER COUNT OF THE MODEL. INF.T INDICATES INFERENCE TIME PER IMAGE. THE BEST TWO RESULTS ARE HIGHLIGHTED IN **BLACK** AND MARK.

Method	O	S	Params.	Inf.T↓	BD↑	HB↑	OT↑	PG↑	AP↑	WT↑	AP <sub>50</sub> ↑	AP <sub>75</sub> ↑	mAP↑
R-FCOS [13]	✓	×	31.9M	17.6ms	32.8	79.8	29.7	67.0	78.9	54.8	57.2	26.4	30.2
R-ATSS [14]	✓	×	36.0M	19.1ms	33.2	80.0	29.3	66.6	78.3	54.8	57.0	27.1	30.0
YOLOv5 [40]	✓	×	8.10M	7.20ms	61.4	88.0	56.6	76.4	91.3	91.8	77.6	59.8	52.9
Roi-Trans [54]	✓	×	273M	49.3ms	17.2	80.7	9.1	55.2	80.5	25.6	44.2	27.6	27.1
O-RepPoint [55]	✓	×	36.6M	16.1ms	63.3	90.2	55.8	81.7	88.2	90.1	77.1	58.3	53.9
RTMDet [56]	✓	×	8.86M	11.1ms	34.0	79.8	30.3	61.1	79.1	55.9	56.7	26.5	29.2
YOLOv8 [40]	✓	×	10.0M	6.70ms	63.6	88.6	57.9	80.0	91.3	92.5	79.0	61.6	54.4
PSC [57]	✓	×	31.9M	18.3ms	30.7	79.7	25.9	57.4	78.1	49.4	53.5	26.2	28.5
KFloU [58]	✓	×	36.2M	66.2ms	16.9	79.4	9.1	50.9	80.4	25.2	43.6	19.4	22.4
YOLOv6 [41]	✓	×	16.0M	6.10ms	57.6	82.1	52.7	67.6	89.4	90.4	73.3	64.9	48.8
YOLOv9 [42]	✓	×	6.40M	14.4ms	61.9	87.7	55.3	74.4	90.0	92.4	76.9	58.9	52.5
YOLOv10 [43]	✓	×	7.50M	7.80ms	65.2	89.9	58.8	82.3	90.8	93.5	80.1	62.8	55.7
YOLOv11 [40]	✓	×	9.74M	6.50ms	64.3	90.0	57.8	80.7	90.9	91.5	79.2	60.5	54.3
LSKNet [1]	✓	×	21.8M	20.4ms	63.3	90.2	55.8	81.7	88.2	90.1	77.1	58.3	53.9
YOLOv12 [59]	✓	×	9.36M	13.4ms	62.7	88.6	57.1	80.1	91.0	92.7	78.7	61.1	54.0
R-FCOS [13]	×	✓	31.9M	17.6ms	23.9	80.1	27.9	60.1	75.8	43.5	51.9	26.4	28.3
R-ATSS [14]	×	✓	36.0M	19.1ms	25.3	80.3	26.8	62.3	77.0	43.9	52.6	24.9	27.8
YOLOv5 [40]	×	✓	8.10M	7.20ms	40.5	85.3	41.0	64.3	85.5	89.9	67.7	44.0	41.3
Roi-Trans [54]	×	✓	273M	49.3ms	9.1	80.8	9.1	35.6	79.0	18.0	38.6	25.2	24.3
O-RepPoint [55]	×	✓	36.6M	16.1ms	26.2	78.6	21.9	53.7	59.9	48.8	48.2	13.9	20.4
RTMDet [56]	×	✓	8.86M	11.1ms	16.2	71.0	21.1	39.3	68.9	39.6	42.7	20.9	22.3
YOLOv8 [40]	×	✓	10.0M	6.70ms	44.9	85.8	42.5	67.9	87.5	89.2	69.6	46.1	43.2
PSC [57]	×	✓	31.9M	18.3ms	22.3	80.0	20.6	51.9	75.7	39.4	48.3	24.5	26.5
KFloU [58]	×	✓	36.2M	66.2ms	9.1	72.1	9.1	35.3	78.0	22.7	37.7	17.4	19.8
YOLOv6 [41]	×	✓	16.0M	6.10ms	36.5	79.4	32.8	53.5	85.7	86.7	62.4	37.6	36.5
YOLOv9 [42]	×	✓	6.40M	14.4ms	43.9	84.8	38.4	61.5	87.9	88.8	67.6	44.2	41.4
YOLOv10 [43]	×	✓	7.50M	7.80ms	49.8	87.0	45.5	73.4	87.9	90.4	72.3	50.8	46.2
YOLOv11 [40]	×	✓	9.74M	6.50ms	46.9	87.2	44.6	71.1	88.8	89.2	71.3	48.6	44.7
LSKNet [1]	×	✓	21.8M	20.4ms	33.4	80.2	28.4	69.3	76.8	51.2	56.6	27.1	30.4
YOLOv12 [59]	×	✓	9.36M	13.0ms	46.4	87.7	43.6	70.8	90.0	90.7	71.5	49.2	45.4
CFT [28]	✓	✓	53.8M	40.6ms	75.8	<u>92.5</u>	<u>61.3</u>	91.6	90.3	96.3	84.6	68.9	59.9
COMO [60]	✓	✓	22.6M	37.1ms	72.3	90.8	60.4	88.7	90.5	96.3	83.2	66.3	57.9
CLANet [17]	✓	✓	48.2M	29.1ms	74.8	92.2	60.7	91.3	91.6	<u>97.2</u>	84.6	68.5	59.6
CSSA [18]	✓	✓	13.5M	12.3ms	73.3	91.7	59.3	88.9	91.6	95.8	83.4	66.4	58.0
CMADet [29]	✓	✓	41.5M	46.7ms	70.9	90.7	52.0	86.4	91.7	97.1	81.5	63.5	55.7
ICAFusion [30]	✓	✓	29.0M	23.6ms	74.7	91.9	60.9	91.0	<u>91.8</u>	96.7	84.5	67.3	58.8
MMIDet [31]	✓	✓	53.8M	41.9ms	74.9	<b>92.6</b>	61.1	<u>91.7</u>	91.4	97.0	84.8	68.6	59.8
E2E-MFD [49]	✓	✓	31.3M	37.1ms	76.1	91.9	61.1	<b>91.8</b>	91.3	<u>97.2</u>	84.9	69.5	60.5
<b>E2E-OSDet (Ours)</b>	✓	✓	24.7M	20.9ms	<b>77.7</b>	90.7	<b>64.3</b>	<b>91.8</b>	<b>92.1</b>	<b>97.8</b>	<b>85.7</b>	<b>70.3</b>	<b>61.4</b>

4) *Area-attention Fusion Module*: To enhance the discriminative capacity of fused optical-SAR features across spatially diverse regions, we propose the Area-attention Fusion Module (AFM), a novel mechanism that emphasizes salient local structures and amplifies responses in critical target regions. AFM exploits the complementary characteristics of optical and SAR modalities, enabling robust and adaptive feature integration for multi-source object detection. Inspired by the efficient spatial modeling techniques in [59], [61], AFM partitions the input feature map of resolution  $(H, W)$  into  $k$  non-overlapping blocks of size  $(H/k, W)$  or  $(H, W/k)$ , without requiring explicit window segmentation. This lightweight partitioning is implemented via a simple reshaping operation, preserving spatial continuity while substantially improving computational efficiency. The fused feature representation is computed as:

$$F_j^{fus} = \text{AFM}(F'_{Oj}, F'_{Sj}), \quad j \in \{3, 4, 5\}, \quad (10)$$

where  $F'_{Oj}$  and  $F'_{Sj}$  denote the optical and SAR features. By adaptively weighting localized features, AFM improves the model's capability to detect targets in complex remote sensing scenes characterized by varying object scales and cluttered backgrounds. As illustrated in Fig. 4 (c), AFM achieves effi-

cient and effective cross-modal fusion, surpassing conventional spatial fusion strategies that often overlook regional saliency and incur higher computational overhead.

### C. Loss Function

In the proposed E2E-OSDet framework, we employ a composite loss function comprising Binary Cross-Entropy (BCE) and Probabilistic IoU (ProbIoU) [62] to jointly optimize classification and localization. The overall loss is defined as:

$$\mathcal{L}_{total} = \mathcal{L}_{reg} + \mathcal{L}_{dfl} + \mathcal{L}_{cls}, \quad (11)$$

where  $\mathcal{L}_{reg}$  denotes the bounding box regression loss,  $\mathcal{L}_{dfl}$  represents the distribution focus loss, and  $\mathcal{L}_{cls}$  corresponds to the classification loss. This formulation balances localization accuracy and classification confidence, ensuring end-to-end optimization of the optical-SAR fusion detection pipeline.

## V. M4-SAR BENCHMARK

### A. Setups and Implementation Details

Experiments were conducted on two NVIDIA RTX 4090 GPUs. All fusion models were trained over 300 epochs with

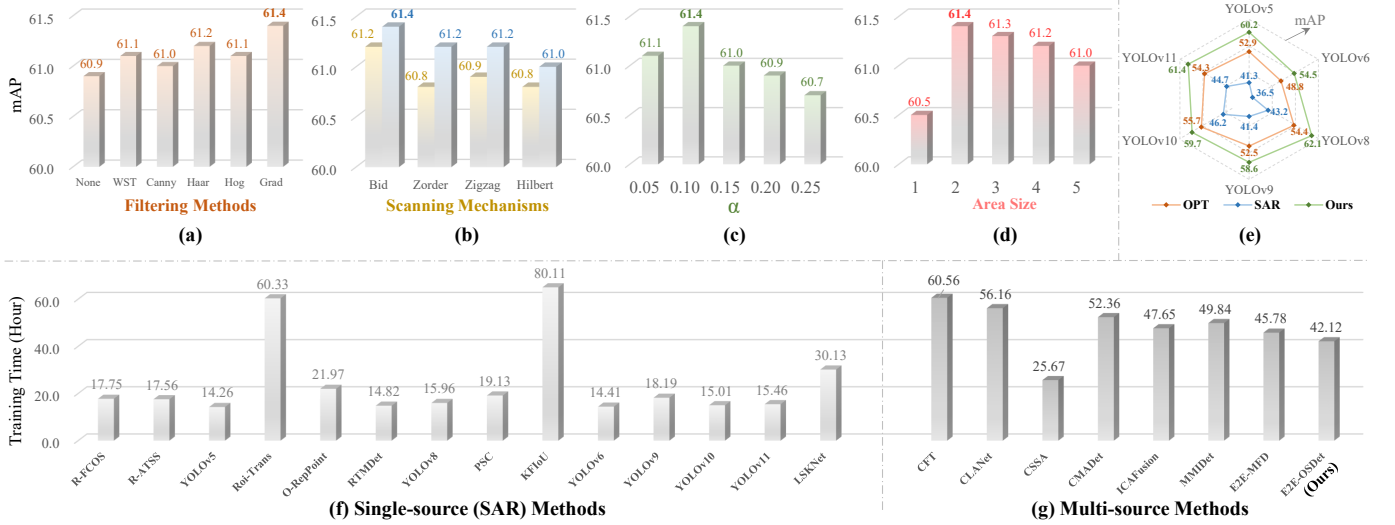


Fig. 6. (a) Effect of different handcrafted features. (b) Effect of different scanning mechanisms. (c) Effect of varying ratios of handcrafted features. (d) Effect of different attention regions. (e) Performance of E2E-OSDet across various detectors. (f) Training time of the single-source method (using SAR images). (g) Training time of the multi-source method (using optical and SAR images).

TABLE III  
ABLATION ANALYSIS OF E2E-OSDET ON M4-SAR DATASET.

No.	FAM	CMIM	AFM	Train-Params.	$AP_{50} \uparrow$	$AP_{75} \uparrow$	$mAP \uparrow$
(a)	×	×	×	14.17M baseline	83.4	66.4	58.0
(b)	✓	×	×	14.17M +0M	84.5	67.1	58.9
(c)	×	✓	×	19.01M +5.68M	84.9	68.6	59.6
(d)	×	×	✓	19.84M +4.84M	84.6	68.9	60.0
(e)	✓	✓	×	19.84M +4.84M	85.5	69.9	61.0
(f)	✓	×	✓	19.01M +5.68M	84.9	69.5	60.7
(g)	×	✓	✓	24.69M +10.52M	85.2	70.0	60.9
(h)	✓	✓	✓	24.69M +10.52M	<b>85.7</b>	<b>70.3</b>	<b>61.4</b>

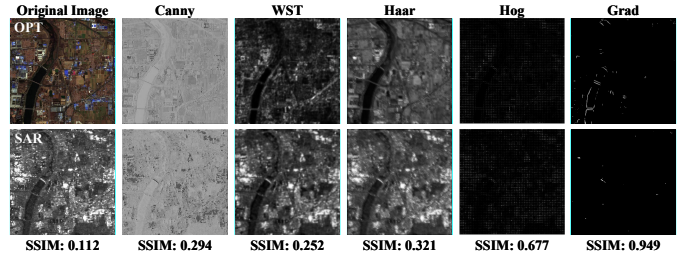


Fig. 7. Visualization results of handcrafted features.

the SGD optimizer, using a learning rate of 0.01, momentum of 0.937, and weight decay of  $5 \times 10^{-4}$ . The batch size was set to 64, and the input images were resized to a resolution of  $512 \times 512$ . To ensure fair performance evaluation, all methods were evaluated using a unified framework comprising the YOLOv11 [40] backbone and the oriented detection head from YOLOv8 [40]. These fusion models were trained from scratch, without leveraging any pre-trained weights.

We also evaluate single-source baselines implemented via the MMRotate toolkit [63], including Rotated FCOS [13], Rotated ATSS [14], Oriented R-CNN [64], Oriented RepPoints [55], RTMDet [56], PSC [57], and LSKNet [1]. These methods use a ResNet-50 backbone [65] pre-trained on ImageNet, and are optimized using AdamW [66] (learning rate:  $2e-4$ , weight decay: 0.05) for 72 epochs with a batch size of 32 and the same  $512 \times 512$  input resolution. During evaluation, we adopted the standard COCO evaluation protocol to measure Average Precision (AP), including  $AP_{50}$ ,  $AP_{75}$ , and  $mAP$ .

## B. Main Results

We first compared multi-source fusion methods (such as CFT, CLANet, CSSA, CMADet, ICAFusion, MMIDet, and E2E-MFD) with single-source detection methods (such as R-FCOS, R-ATSS, Roi-Trans, O-RepPoint, RTMDet, and the YOLO series). Experimental results (see Table II) indicate

that detection accuracy using SAR images alone is significantly lower than when using optical images alone. This gap primarily stems from the unique imaging mechanism of SAR: even when targets are visible in the image, SAR struggles to accurately estimate the shape of target bounding boxes.

In contrast, all multi-source fusion methods outperform their corresponding single-modal baselines, clearly demonstrating that cross-modal fusion effectively leverages the complementarity between SAR and optical data to significantly reduce false positives and enhance detection accuracy. Among these, our proposed E2E-OSDet achieves the highest performance across all fusion methods, with a  $mAP$  of 61.4%, fully validating the importance of mitigating domain differences in cross-modal detection. Furthermore, E2E-OSDet exhibits high efficiency with only 24.7M parameters and achieves an inference speed of 20.9ms. We also evaluated its generalization capability across different detection frameworks (see Fig. 6 (e)), demonstrating strong transferability and robustness.

## C. Ablation Experiment

As shown in Table III (a), we adopt CSSA [18] as our baseline model, which serves as the foundation for independently evaluating the contribution of each proposed module. The results (see Table III (a), (b), and (c)) indicate that all three modules lead to performance gains, among which the

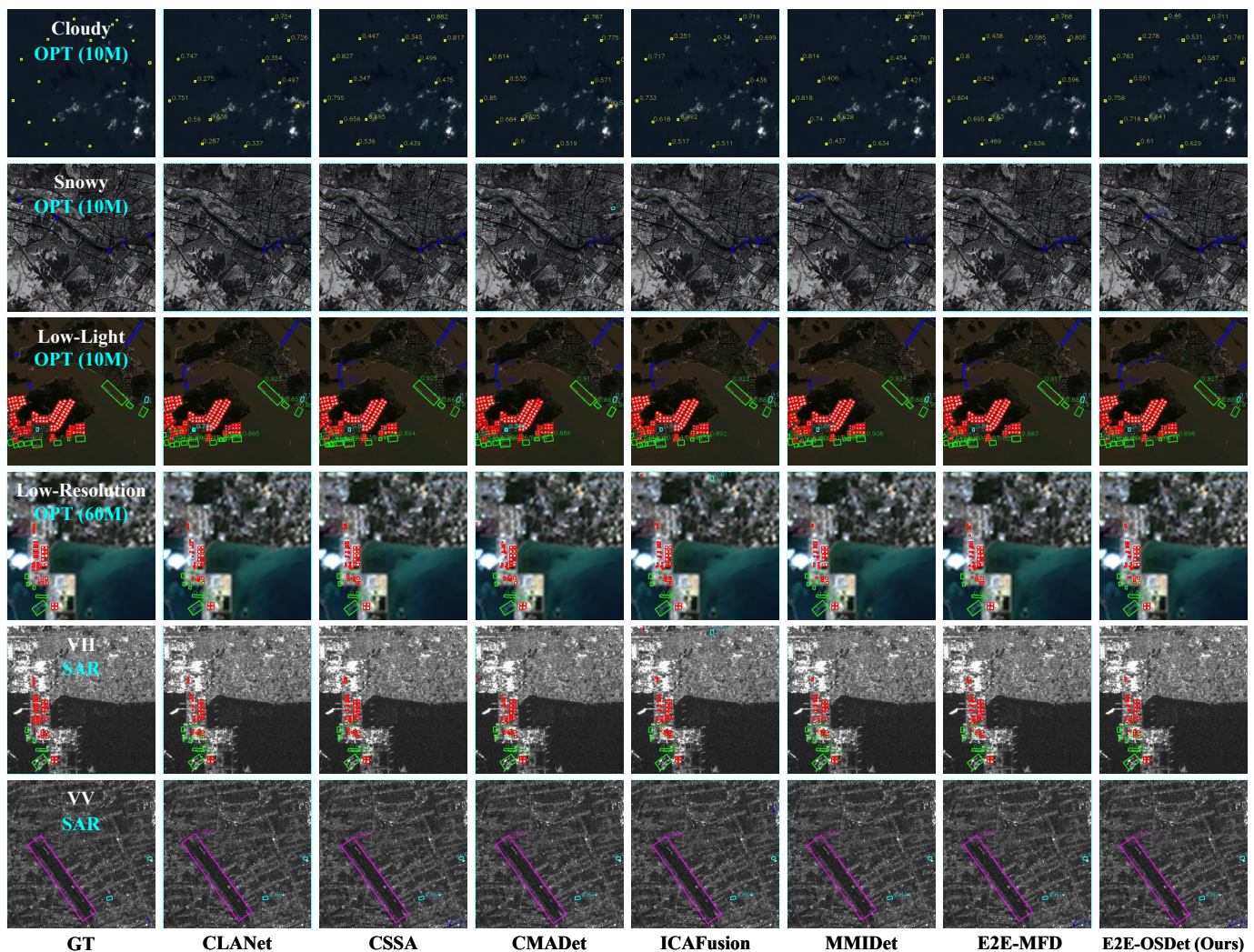


Fig. 8. Qualitative comparison between the proposed E2E-OSDet and six fusion detection methods on the proposed M4-SAR dataset.

AFM module provides the most substantial improvement in detection accuracy. We further assess the interoperability of the modules. As shown in Table III (e), (f), and (g), the modules are compatible with one another, and their integration does not result in any performance degradation. Finally, we integrate all modules (see Table III (h)), resulting in additional gains in overall model performance.

1) *Impact of Filter Augment*: To assess the effectiveness of the FAM, we tested a range of conventional feature descriptors. As shown in Fig. 6 (a) and Fig. 7, the results indicate that incorporating handcrafted features significantly enhances detection performance. These results mapping pixels into a handcrafted feature space effectively reduces the distribution gap between optical and SAR data. Notably, the Grad feature yields superior performance due to its ability to narrow domain differences and capture multi-scale information.

2) *Impact of Scanning Mechanisms*: We further investigate the effectiveness of the CMIM module under different scanning mechanisms [67]. As illustrated in Fig. 6 (b), CMIM consistently enhances detection accuracy regardless of the underlying scanning strategy. This observation highlights the

robustness and adaptability of CMIM, suggesting that the proposed module can serve as a versatile component that generalizes well across diverse architectural settings rather than being restricted to a particular scanning design.

3) *Impact of Feature Proportion and Area Size*: In addition, we investigate the influence of two key design choices: the proportion of handcrafted feature input and the adoption of area attention. As shown in Fig. 6 (c) and (d), varying these hyperparameters leads to only marginal performance differences, indicating that the overall framework is relatively insensitive to such configurations. This stability suggests that our method achieves consistent performance without requiring delicate hyperparameter tuning, further underscoring its practicality in real-world deployment.

#### D. Qualitative Evaluation

We present visual comparisons of detection results from various multi-source methods. As shown in Fig. 8, the proposed E2E-OSDet consistently outperforms other methods in complex scenes. In particular, in regions with limited optical information, such as cloud-covered, snow-covered,

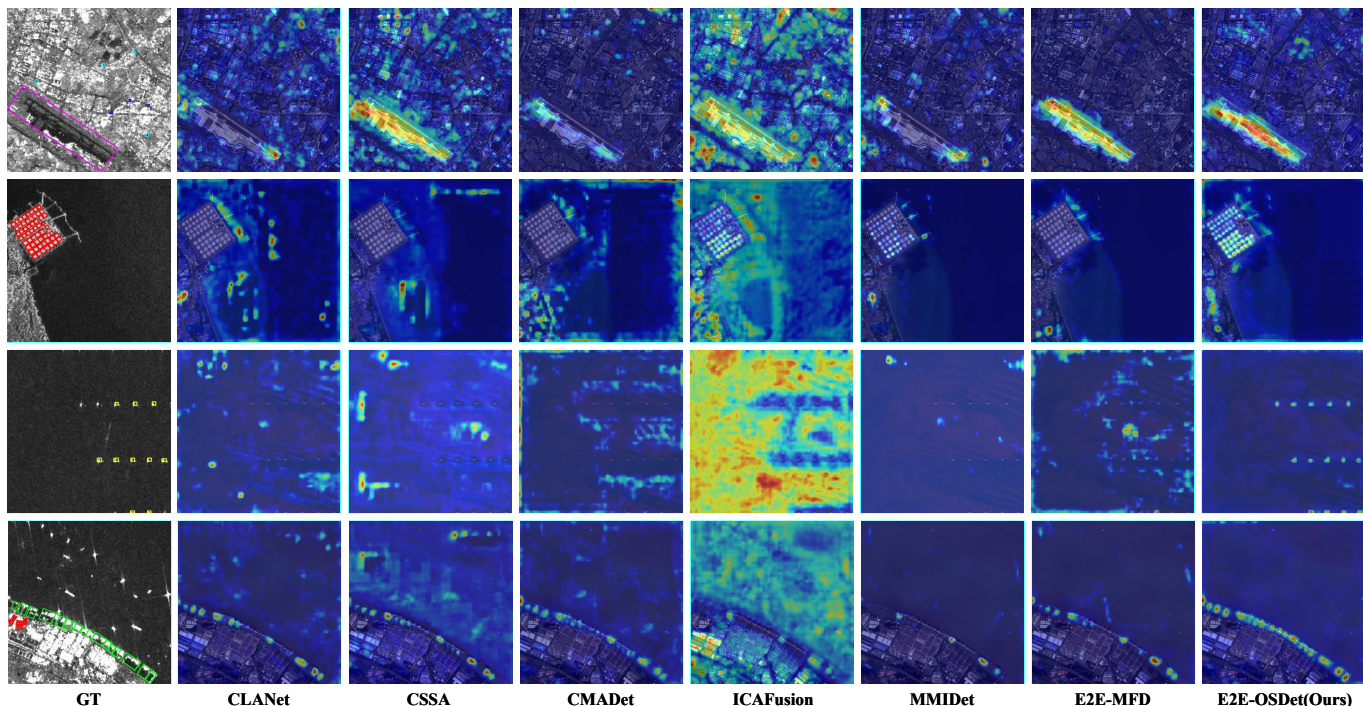


Fig. 9. Grad-CAM [68] heatmaps of the proposed E2E-OSDet and six fusion detection methods on the proposed M4-SAR dataset.

low-light, or low-resolution areas, the incorporation of SAR data significantly enhances target localization accuracy. As illustrated in Fig. 9, our proposed E2E-OSDet produces highly concentrated and spatially aligned attention maps, accurately focusing on target regions while suppressing irrelevant background activations. These experimental results demonstrate the proposed dataset’s effectiveness in evaluating the robustness and adaptability of detection models across diverse scenarios.

## VI. DISCUSSIONS

### A. Expanded Application of E2E-OSDet

To further assess the generalization capability of the E2E-OSDet framework, we conducted additional experiments on the OGSOD-1.0 [24] and OGSOD-2.0 [25] datasets (300 epochs, input resolution of  $256 \times 256$ ). As shown in Table IV, E2E-OSDet attains the highest performance on OGSOD-1.0, achieving an  $mAP$  of 67.3% and surpassing representative multimodal methods, including CLANet, ICAFusion, and MMIDet. These results demonstrate the robustness and generalizability of E2E-OSDet across various benchmarks.

### B. Limitations Analysis of M4-SAR

Despite the substantial advantages of M4-SAR in terms of scale, diversity, and scene coverage, certain limitations persist that require further exploration. First, a temporal misalignment often occurs between the acquisition of optical and SAR images, which may cause spatial inconsistencies for certain dynamic targets. Second, the dataset is currently limited to six representative static categories and does not yet include more dynamic or fine-grained object classes. Third, although

TABLE IV  
QUANTITATIVE RESULTS ON THE OGSOD-1.0 AND OGSOD-2.0.

Method	O	S	OGSOD-1.0 [24]			OGSOD-2.0 [25]		
			AP <sub>50</sub>	AP <sub>75</sub>	mAP	AP <sub>50</sub>	AP <sub>75</sub>	mAP
YOLOv11 [40]	✓	✗	90.8	66.0	61.5	88.2	62.6	58.5
YOLOv11 [40]	✗	✓	76.0	48.0	47.8	73.8	46.2	45.9
CFT [28]	✓	✓	92.9	72.1	65.3	90.8	67.1	61.4
CLANet [17]	✓	✓	93.5	72.9	66.3	91.6	68.7	63.0
CSSA [18]	✓	✓	92.1	69.3	63.3	89.7	64.2	59.8
CMADet [29]	✓	✓	91.3	67.6	62.9	88.1	60.9	57.7
ICAFusion [30]	✓	✓	93.5	72.7	66.1	90.7	68.2	62.2
MMIDet [31]	✓	✓	93.5	73.5	66.7	91.6	68.6	63.0
<b>E2E-OSDet</b>	✓	✓	<b>93.6</b>	<b>74.3</b>	<b>67.3</b>	<b>92.3</b>	<b>71.8</b>	<b>65.1</b>

E2E-OSDet provides a robust performance baseline, its computational demands still present challenges for deployment on resource-constrained edge devices.

### C. Future Work

M4-SAR offers a high-quality benchmark for optical-SAR fusion detection, with E2E-OSDet delivering superior performance both within this dataset and in cross-dataset evaluations. Future research could investigate the following directions: 1. Broadening the dataset categories to include dynamic and fine-grained targets. 2. Developing lightweight network architectures for edge deployment compatibility. 3. Implementing temporal alignment and multimodal temporal modeling to address cross-modal acquisition time disparities.

## VII. CONCLUSION

This paper presents the M4-SAR dataset and the E2E-OSDet method to tackle two persistent challenges in optical-SAR fusion object detection: the scarcity of high-quality,

large-scale datasets and the absence of a unified and effective algorithmic framework. We also develop MSRODet, a comprehensive open-source toolkit for multi-source rotated object detection that integrates mainstream fusion detection algorithms and enables fair performance comparisons on the M4-SAR dataset. We expect that M4-SAR, as a benchmark dataset, will substantially advance research in multi-source remote sensing detection, while E2E-OSDet, as the first fusion framework specifically designed for optical-SAR scenarios, will serve as a strong baseline for future studies.

## REFERENCES

- [1] Y. Li, X. Li, Y. Dai, Q. Hou, L. Liu, Y. Liu, M.-M. Cheng, and J. Yang, "Lsknet: A foundation lightweight backbone for remote sensing," *International Journal of Computer Vision*, pp. 1–22, 2024.
- [2] W. Lu, S.-B. Chen, C. H. Ding, J. Tang, and B. Luo, "Lwganet: A lightweight group attention backbone for remote sensing visual tasks," *arXiv preprint arXiv:2501.10040*, 2025.
- [3] C. Wang, W. Fang, X. Li, J. Yang, and L. Luo, "Msod: A large-scale multiscene dataset and a novel diagonal-geometry loss for sar object detection," *IEEE Transactions on Geoscience and Remote Sensing*, vol. 63, pp. 1–13, 2025.
- [4] X. Li, Z. Du, Y. Huang, and Z. Tan, "A deep translation (gan) based change detection network for optical and sar remote sensing images," *ISPRS Journal of Photogrammetry and Remote Sensing*, vol. 179, pp. 14–34, 2021.
- [5] C. Zhang, Y. Feng, L. Hu, D. Tapete, L. Pan, Z. Liang, F. Cigna, and P. Yue, "A domain adaptation neural network for change detection with heterogeneous optical and sar remote sensing images," *International Journal of Applied Earth Observation and Geoinformation*, vol. 109, p. 102769, 2022.
- [6] Z. Liu, L. Yuan, L. Weng, and Y. Yang, "A high resolution optical satellite image dataset for ship recognition and some new baselines," in *International Conference on Pattern Recognition Applications and Methods*, vol. 2. SciTePress, 2017, pp. 324–331.
- [7] Z. Zou and Z. Shi, "Random access memories: A new paradigm for target detection in high resolution aerial remote sensing images," *IEEE Transactions on Image Processing*, vol. 27, no. 3, pp. 1100–1111, 2017.
- [8] G. Cheng, J. Wang, K. Li, X. Xie, C. Lang, Y. Yao, and J. Han, "Anchor-free oriented proposal generator for object detection," *IEEE Transactions on Geoscience and Remote Sensing*, vol. 60, pp. 1–11, 2022.
- [9] J. Ding, N. Xue, G.-S. Xia, X. Bai, W. Yang, M. Y. Yang, S. Belongie, J. Luo, M. Datcu, M. Pelillo *et al.*, "Object detection in aerial images: A large-scale benchmark and challenges," *IEEE Transactions on Pattern Analysis and Machine Intelligence*, vol. 44, no. 11, pp. 7778–7796, 2021.
- [10] Y. Li, X. Li, W. Li, Q. Hou, L. Liu, M.-M. Cheng, and J. Yang, "Sardet-100k: Towards open-source benchmark and toolkit for large-scale sar object detection," *arXiv preprint arXiv:2403.06534*, 2024.
- [11] X. Zhang, X. Yang, Y. Li, J. Yang, M.-M. Cheng, and X. Li, "Rsar: Restricted state angle resolver and rotated sar benchmark," *arXiv preprint arXiv:2501.04440*, 2025.
- [12] Y. Wu, Y. Suo, Q. Meng, W. Dai, T. Miao, W. Zhao, Z. Yan, W. Diao, G. Xie, Q. Ke *et al.*, "Fair-csar: A benchmark dataset for fine-grained object detection and recognition based on single look complex sar images," *IEEE Transactions on Geoscience and Remote Sensing*, 2024.
- [13] Z. Tian, C. Shen, H. Chen, and T. He, "Fcos: Fully convolutional one-stage object detection," in *Proceedings of the IEEE/CVF International Conference on Computer Vision*, 2019, pp. 9627–9636.
- [14] S. Zhang, C. Chi, Y. Yao, Z. Lei, and S. Z. Li, "Bridging the gap between anchor-based and anchor-free detection via adaptive training sample selection," in *Proceedings of the IEEE/CVF Conference on Computer Vision and Pattern Recognition*, 2020, pp. 9759–9768.
- [15] Y. Sun, J. Yang, and L. Luo, "United domain cognition network for salient object detection in optical remote sensing images," *IEEE Transactions on Geoscience and Remote Sensing*, vol. 62, pp. 1–14, 2024.
- [16] Y. Sun, C. Wang, J. Yang, and L. Luo, "Small but mighty: Dynamic wavelet expert-guided fine-tuning of large-scale models for optical remote sensing object segmentation," *AAAI Conference on Artificial Intelligence (AAAI)*, 2025.
- [17] X. He, C. Tang, X. Zou, and W. Zhang, "Multispectral object detection via cross-modal conflict-aware learning," in *Proceedings of the 31st ACM International Conference on Multimedia*, 2023, pp. 1465–1474.
- [18] Y. Cao, J. Bin, J. Hamari, E. Blasch, and Z. Liu, "Multimodal object detection by channel switching and spatial attention," in *Proceedings of the IEEE/CVF Conference on Computer Vision and Pattern Recognition*, 2023, pp. 403–411.
- [19] S. Wei, X. Zeng, Q. Qu, M. Wang, H. Su, and J. Shi, "Hrsid: A high-resolution sar images dataset for ship detection and instance segmentation," *IEEE Access*, vol. 8, pp. 120 234–120 254, 2020.
- [20] P. Zhang, H. Xu, T. Tian, P. Gao, L. Li, T. Zhao, N. Zhang, and J. Tian, "Sefepnet: Scale expansion and feature enhancement pyramid network for sar aircraft detection with small sample dataset," *IEEE Journal of Selected Topics in Applied Earth Observations and Remote Sensing*, vol. 15, pp. 3365–3375, 2022.
- [21] T. Zhang, X. Zhang, J. Li, X. Xu, B. Wang, X. Zhan, Y. Xu, X. Ke, T. Zeng, H. Su *et al.*, "Sar ship detection dataset (ssdd): Official release and comprehensive data analysis," *Remote Sensing*, vol. 13, no. 18, p. 3690, 2021.
- [22] X. Lin, B. Zhang, F. Wu, C. Wang, Y. Yang, and H. Chen, "Sived: A sar image dataset for vehicle detection based on rotatable bounding box," *Remote Sensing*, vol. 15, no. 11, p. 2825, 2023.
- [23] Y. Wang, C. Wang, H. Zhang, Y. Dong, and S. Wei, "A sar dataset of ship detection for deep learning under complex backgrounds," *Remote Sensing*, vol. 11, no. 7, p. 765, 2019.
- [24] C. Wang, R. Ruan, Z. Zhao, C. Li, and J. Tang, "Category-oriented localization distillation for sar object detection and a unified benchmark," *IEEE Transactions on Geoscience and Remote Sensing*, vol. 61, pp. 1–14, 2023.
- [25] C. Wang, L. Luo, W. Fang, and J. Yang, "Cross-modal gaussian localization distillation for optical information guided sar object detection," in *ICASSP 2025-2025 IEEE International Conference on Acoustics, Speech and Signal Processing (ICASSP)*. IEEE, 2025, pp. 1–5.
- [26] R. Torres, P. Snoeij, D. Geudtner, D. Bibby, M. Davidson, E. Attema, P. Potin, B. Rommen, N. Floury, M. Brown *et al.*, "Gmes sentinel-1 mission," *Remote Sensing of Environment*, vol. 120, pp. 9–24, 2012.
- [27] M. Drusch, U. Del Bello, S. Carlier, O. Colin, V. Fernandez, F. Gascon, B. Hoersch, C. Isola, P. Laberinti, P. Martimort *et al.*, "Sentinel-2: Esa's optical high-resolution mission for gmes operational services," *Remote Sensing of Environment*, vol. 120, pp. 25–36, 2012.
- [28] F. Qingyun and W. Zhaokui, "Cross-modality attentive feature fusion for object detection in multispectral remote sensing imagery," *Pattern Recognition*, vol. 130, p. 108786, 2022.
- [29] K. Song, X. Xue, H. Wen, Y. Ji, Y. Yan, and Q. Meng, "Misaligned visible-thermal object detection: a drone-based benchmark and baseline," *IEEE Transactions on Intelligent Vehicles*, 2024.
- [30] J. Shen, Y. Chen, Y. Liu, X. Zuo, H. Fan, and W. Yang, "Icafusion: Iterative cross-attention guided feature fusion for multispectral object detection," *Pattern Recognition*, vol. 145, p. 109913, 2024.
- [31] Y. Zeng, T. Liang, Y. Jin, and Y. Li, "Mmi-det: Exploring multi-modal integration for visible and infrared object detection," *IEEE Transactions on Circuits and Systems for Video Technology*, 2024.
- [32] R. Xia, J. Chen, Z. Huang, H. Wan, B. Wu, L. Sun, B. Yao, H. Xiang, and M. Xing, "Crtranssar: A visual transformer based on contextual joint representation learning for sar ship detection," *Remote Sensing*, vol. 14, no. 6, p. 1488, 2022.
- [33] J. Canny, "A computational approach to edge detection," *IEEE Transactions on Pattern Analysis and Machine Intelligence*, no. 6, pp. 679–698, 1986.
- [34] S. Mallat, "Group invariant scattering," *Communications on Pure and Applied Mathematics*, vol. 65, no. 10, pp. 1331–1398, 2012.
- [35] P. Viola and M. Jones, "Rapid object detection using a boosted cascade of simple features," in *Proceedings of the IEEE/CVF Conference on Computer Vision and Pattern Recognition*, vol. 1. Ieee, 2001, pp. I–I.
- [36] N. Dalal and B. Triggs, "Histograms of oriented gradients for human detection," in *Proceedings of the IEEE/CVF Conference on Computer Vision and Pattern Recognition*, vol. 1. Ieee, 2005, pp. 886–893.
- [37] W. Li, W. Yang, T. Liu, Y. Hou, Y. Li, Z. Liu, Y. Liu, and L. Liu, "Predicting gradient is better: Exploring self-supervised learning for sar atr with a joint-embedding predictive architecture," *ISPRS Journal of Photogrammetry and Remote Sensing*, vol. 218, pp. 326–338, 2024.
- [38] R. Girshick, "Fast r-cnn," in *Proceedings of the IEEE/CVF International Conference on Computer Vision*, 2015, pp. 1440–1448.
- [39] K. He, G. Gkioxari, P. Dollár, and R. Girshick, "Mask r-cnn," in *Proceedings of the IEEE/CVF International Conference on Computer Vision*, 2017, pp. 2961–2969.
- [40] G. Jocher, J. Qiu, and A. Chaurasia, "Ultralytics YOLO," Jan. 2023. [Online]. Available: <https://github.com/ultralytics/ultralytics>

- [41] C. Li, L. Li, H. Jiang, K. Weng, Y. Geng, L. Li, Z. Ke, Q. Li, M. Cheng, W. Nie *et al.*, “Yolov6: A single-stage object detection framework for industrial applications,” *arXiv preprint arXiv:2209.02976*, 2022.
- [42] C.-Y. Wang, I.-H. Yeh, and H.-Y. Mark Liao, “Yolov9: Learning what you want to learn using programmable gradient information,” in *European Conference on Computer Vision*. Springer, 2024, pp. 1–21.
- [43] A. Wang, H. Chen, L. Liu, K. Chen, Z. Lin, J. Han, and G. Ding, “Yolov10: Real-time end-to-end object detection. arxiv 2024,” *arXiv preprint arXiv:2405.14458*, 2024.
- [44] K. Li, D. Wang, Z. Hu, W. Zhu, S. Li, and Q. Wang, “Unleashing channel potential: Space-frequency selection convolution for sar object detection,” in *Proceedings of the IEEE/CVF Conference on Computer Vision and Pattern Recognition*, 2024, pp. 17 323–17 332.
- [45] J. Li, X. Wang, H. Zhao, and Y. Zhong, “Learning a cross-modality anomaly detector for remote sensing imagery,” *IEEE Transactions on Image Processing*, 2024.
- [46] J. Wang, Z. Cui, T. Jiang, C. Cao, and Z. Cao, “Lightweight deep neural networks for ship target detection in sar imagery,” *IEEE Transactions on Image Processing*, vol. 32, pp. 565–579, 2022.
- [47] W. Li, W. Yang, Y. Hou, L. Liu, Y. Liu, and X. Li, “Saratr-x: Towards building a foundation model for sar target recognition,” *IEEE Transactions on Image Processing*, 2025.
- [48] M. Yuan, Y. Wang, and X. Wei, “Translation, scale and rotation: cross-modal alignment meets rgb-infrared vehicle detection,” in *European Conference on Computer Vision*. Springer, 2022, pp. 509–525.
- [49] J. Zhang, M. Cao, X. Yang, W. Xie, J. Lei, D. Li, G. Yang, W. Huang, and Y. Li, “E2e-mfd: Towards end-to-end synchronous multimodal fusion detection,” in *Neural Information Processing Systems*, 2024.
- [50] A. Gu and T. Dao, “Mamba: Linear-time sequence modeling with selective state spaces,” *arXiv preprint arXiv:2312.00752*, 2023.
- [51] Y. Zhan, Z. Zeng, H. Liu, X. Tan, and Y. Tian, “Mambasod: Dual mamba-driven cross-modal fusion network for rgb-d salient object detection,” *Neurocomputing*, vol. 631, p. 129718, 2025.
- [52] W. Dong, H. Zhu, S. Lin, X. Luo, Y. Shen, X. Liu, J. Zhang, G. Guo, and B. Zhang, “Fusion-mamba for cross-modality object detection,” *arXiv preprint arXiv:2404.09146*, 2024.
- [53] X. Hu, Y. Tai, X. Zhao, C. Zhao, Z. Zhang, J. Li, B. Zhong, and J. Yang, “Exploiting multimodal spatial-temporal patterns for video object tracking,” in *Proceedings of the AAAI Conference on Artificial Intelligence*, vol. 39, no. 4, 2025, pp. 3581–3589.
- [54] T. Ma, M. Mao, H. Zheng, P. Gao, X. Wang, S. Han, E. Ding, B. Zhang, and D. Doermann, “Oriented object detection with transformer,” *arXiv preprint arXiv:2106.03146*, 2021.
- [55] W. Li, Y. Chen, K. Hu, and J. Zhu, “Oriented reppoints for aerial object detection,” in *Proceedings of the IEEE/CVF Conference on Computer Vision and Pattern Recognition*, 2022, pp. 1829–1838.
- [56] C. Lyu, W. Zhang, H. Huang, Y. Zhou, Y. Wang, Y. Liu, S. Zhang, and K. Chen, “Rtmdet: An empirical study of designing real-time object detectors,” *arXiv preprint arXiv:2212.07784*, 2022.
- [57] Y. Yu and F. Da, “Phase-shifting coder: Predicting accurate orientation in oriented object detection,” in *Proceedings of the IEEE/CVF Conference on Computer Vision and Pattern Recognition*, 2023, pp. 13 354–13 363.
- [58] X. Yang, Y. Zhou, G. Zhang, J. Yang, W. Wang, J. Yan, X. Zhang, and Q. Tian, “The kfiou loss for rotated object detection,” *arXiv preprint arXiv:2201.12558*, 2022.
- [59] Y. Tian, Q. Ye, and D. Doermann, “Yolov12: Attention-centric real-time object detectors,” *arXiv preprint arXiv:2502.12524*, 2025.
- [60] C. Liu, X. Ma, X. Yang, Y. Zhang, and Y. Dong, “Como: Cross-mamba interaction and offset-guided fusion for multimodal object detection,” *Information Fusion*, vol. 125, p. 103414, 2026.
- [61] P. Geng, X. Lu, C. Hu, H. Liu, and L. Lyu, “Focusing fine-grained action by self-attention-enhanced graph neural networks with contrastive learning,” *IEEE Transactions on Circuits and Systems for Video Technology*, vol. 33, no. 9, pp. 4754–4768, 2023.
- [62] J. M. Llerena, L. F. Zeni, L. N. Kristen, and C. Jung, “Gaussian bounding boxes and probabilistic intersection-over-union for object detection,” *arXiv preprint arXiv:2106.06072*, 2021.
- [63] MMRotate Contributors, “OpenMMLab rotated object detection toolbox and benchmark,” Feb. 2022. [Online]. Available: <https://github.com/open-mmlab/mmrrotate>
- [64] X. Xie, G. Cheng, J. Wang, X. Yao, and J. Han, “Oriented r-cnn for object detection,” in *Proceedings of the IEEE/CVF International Conference on Computer Vision*, 2021, pp. 3520–3529.
- [65] K. He, X. Zhang, S. Ren, and J. Sun, “Deep residual learning for image recognition,” in *Proceedings of the IEEE/CVF Conference on Computer Vision and Pattern Recognition*, 2016, pp. 770–778.
- [66] I. Loshchilov and F. Hutter, “Decoupled weight decay regularization,” *arXiv preprint arXiv:1711.05101*, 2017.
- [67] H. He, Y. Bai, J. Zhang, Q. He, H. Chen, Z. Gan, C. Wang, X. Li, G. Tian, and L. Xie, “Mambaad: Exploring state space models for multi-class unsupervised anomaly detection,” *arXiv preprint arXiv:2404.06564*, 2024.
- [68] R. R. Selvaraju, M. Cogswell, A. Das, R. Vedantam, D. Parikh, and D. Batra, “Grad-cam: Visual explanations from deep networks via gradient-based localization,” in *Proceedings of the IEEE/CVF International Conference on Computer Vision*, 2017, pp. 618–626.